AGU PUBLICATIONS

JGR

Journal of Geophysical Research: Space Physics

TECHNICAL REPORTS: METHODS

10.1002/2016JA022994

**Key Points:**
- Technique developed to locate cylindrical, quasi force-free flux ropes in magnetometer data
- Method uses wavelet analysis, minimum variance analysis, and a constant-$\alpha$ force-free flux rope model
- Technique successfully applied to MESSENGER data from the Hermean magnetotail

**Correspondence to:**
A. W. Smith,
AW.Smith@soton.ac.uk

**Citation:**
Smith, A. W., J. A. Slavin, C. M. Jackman, R. C. Fear, G.-K. Poh, G. A. DiBraccio, J. M. Jasinski, and L. Trenchi (2017), Automated force free flux rope identification, *J. Geophys. Res. Space Physics*, *122*, 780–791, doi:10.1002/2016JA022994.

Received 24 MAY 2016
Accepted 22 DEC 2016
Accepted article online 29 DEC 2016
Published online 25 JAN 2017



# Automated force-free flux rope identification

**A. W. Smith[1], J. A. Slavin[2], C. M. Jackman[1], R. C. Fear[1], G.-K. Poh[2], G. A. DiBraccio[3], J. M. Jasinski[2], and L. Trenchi[1]**

[1]Department of Physics and Astronomy, University of Southampton, Southampton, UK, [2]Climate and Space Sciences and Engineering, University of Michigan, Ann Arbor, Michigan, USA, [3]Solar System Exploration Division, NASA Goddard Space Flight Center, Greenbelt, Maryland, USA

**Abstract** We describe a method developed to automatically identify quasi force-free magnetotail flux ropes from in situ spacecraft magnetometer data. The method locates significant (greater than $1\sigma$) deflections of the north-south component of the magnetic field coincident with enhancements in other field components. The magnetic field data around the deflections are then processed using Minimum Variance Analysis (MVA) to narrow the selection down to those that exhibit the characteristics of flux ropes. The subset of candidates that fulfills the requirements are then compared to a cylindrical, linear (constant-$\alpha$) force-free model. Those that can be well approximated as force free are then accepted. The model fit also provides a measure of the physical parameters that describe the flux rope (i.e., core field and radius). This process allows for the creation of a repeatable, consistent catalog of flux ropes. Automation allows a greater volume of data to be covered, saving time and allowing the exploration of potential selection biases. The technique is applied to MESSENGER (MErcury Surface, Space ENvironment, GEochemistry, and Ranging) magnetometer data in the Hermean magnetotail and successfully locates flux ropes, some of which match previously known encounters. Assumptions of the method and potential future applications are discussed.

## 1. Introduction

Magnetic reconnection is a ubiquitous process throughout the magnetized plasmas of the solar system. It is a fundamental mechanism by which energy can be transferred from magnetic fields to the surrounding plasma. In the context of a planetary magnetosphere, reconnection is most commonly observed at the magnetopause and in the magnetotail current sheet. Reconnection at the magnetopause can cause mass and flux to be added to the magnetospheric system (from the solar wind), while reconnection of the adjacent antiparallel fields at the magnetotail current sheet can result in the loss of mass and/or magnetic flux from the system.

In two dimensions, the presence of one or more reconnection *x* lines on closed field lines leads to the generation of magnetic islands, or loops [*Schindler*, 1974]. At the center of a magnetic loop the field strength is zero. When considering three-dimensional systems, the formation of magnetic loops requires precisely antiparallel fields. At Earth and Mercury the magnetic fields within the northern and southern lobes of the magnetotail are often found to be sheared: a result of the interaction between the solar wind and the magnetosphere [*Cowley*, 1981]. The presence of a shear generates a component of the magnetic field in the azimuthal direction across the current sheet; this can act as a guide field during reconnection, potentially resulting in the formation of flux ropes [*Hughes and Sibeck*, 1987]; however, this is still an active area of research [e.g., *Borg et al.*, 2012]. Flux rope-type plasmoids consist of a series of nested helical magnetic fields forming a cylindrical structure [*Lepping et al.*, 1990].

On the magnetospheric scale reconnection forms part of a process by which plasma, magnetic flux, and energy can be transported from the dayside magnetopause into the magnetotail known as the Dungey cycle [*Dungey*, 1961]. In this cycle magnetospheric flux is opened at the planet's dayside magnetopause via reconnection with the interplanetary magnetic field in the impinging solar wind. The newly generated open field lines, which map from the planet to the solar wind, are swept across the polar regions into the magnetotail lobes. Meanwhile, reconnection in the magnetotail current sheet can close the oppositely directed lobe fields. The cycle is completed as the closed field lines convect around the flanks to return to the dayside of the planet.

As the closest planet to the Sun, and possessing a relatively small magnetosphere (compared to the other magnetized planets), Mercury is particularly susceptible to variations in the solar wind, changes that can

drive the Dungey cycle. Due to the small spatial scales involved, the cycle operates over dramatically shorter timescales, of the order of ~2 to 3 min [*Siscoe et al.*, 1975; *Slavin et al.*, 2010; *Sun et al.*, 2015], compared to ~1 to 3 h at Earth [*Akasofu*, 1964; *Baker et al.*, 1996; *Huang*, 2002]. Similarly, the average duration of magnetotail flux rope observations with the MESSENGER (MErcury Surface, Space ENvironment, GEochemistry, and Ranging) spacecraft at Mercury was found to be 0.74 s [*DiBraccio et al.*, 2015], much shorter than the 30 s to 2 min durations observed at the Earth [*Ieda et al.*, 1998; *Slavin et al.*, 2003a].

Historically, surveys of plasmoids and flux ropes in Earth's magnetotail have been performed by visual inspection of spacecraft data [e.g., *Scholer et al.*, 1984; *Richardson et al.*, 1987; *Moldwin and Hughes*, 1992; *Ieda et al.*, 1998; *Slavin et al.*, 2003a]. Criteria based on the magnetic field and local plasma environment were developed and applied by eye to create self-consistent catalogs. Similarly, several studies of flux ropes in the magnetotail of Mercury have been performed [*Slavin et al.*, 2009, 2012; *DiBraccio et al.*, 2015]. Unlike at the Earth, where high-resolution plasma data are generally available, these studies have relied more heavily on the magnetometer data to identify these structures. Again, selection criteria were applied manually and each event processed individually. This has worked very well in both environments; however, it is hugely time consuming and difficult to keep the selection process completely consistent; separate authors may well select marginally different subsets of events.

Some studies have begun to introduce some degree of automation to the process of plasmoid identification, e.g., for locating periods when the north-south component of the magnetic field is enhanced above background levels [*Vogt et al.*, 2010; *Jackman et al.*, 2014] or to find significant deflections of the field [*Smith et al.*, 2016]. Automated techniques have also been used to identify magnetopause flux transfer events (FTEs) via bipolar field deflections [e.g., *Kawano and Russell*, 1996], albeit still requiring manual confirmation. *Karimabadi et al.* [2007] introduced a data mining technique (MineTool) and later applied it to locate FTEs [*Karimabadi et al.*, 2009], using a combination of magnetic field and plasma data. Recently, *Malaspina and Gosling* [2012] refined a technique to identify rotational discontinuities in the STEREO solar wind data using the gradient of the magnetic field (the method was initially developed by *Vasquez et al.* [2007]). These techniques are well designed to pick out large scale rotations of a single field component. Flux rope signatures, however, are complex and require coordinated changes in multiple field components.

We present a fully automated technique designed to identify in situ observations of linear (constant $\alpha$) force-free magnetotail flux ropes in spacecraft magnetometer data. The method includes several widely used analysis methods, which when combined consistently identify flux ropes signatures. The automation both reduces the subjectivity of flux rope surveys and enables the application of Minimum Variance Analysis (MVA) and force-free model fitting to large ensembles of flux ropes.

The technique has been developed using MESSENGER magnetometer data; however, it could be applied to other data sets with some adaptation. Below we summarize the dataset used, the expected magnetic field signature in the data and the flux rope model selected. The process is then discussed with reference to an example detection and several trial intervals. Assumptions and potential adaptations are then discussed.

## 2. Data, Signatures, and Model

### 2.1. Data

The method was developed using magnetometer data from the MESSENGER (MErcury Surface, Space ENvironment, GEochemistry, and Ranging) spacecraft [*Solomon et al.*, 2007; *Anderson et al.*, 2007]. Data with a cadence of 20 Hz were used; the short timescales of flux ropes (~0.74 s [*DiBraccio et al.*, 2015]) necessitate the use of high-resolution data. MESSENGER orbited Mercury from 18 March 2011 to 30 April 2015. During this time it performed highly inclined, eccentric orbits with a period of ~12 h (later reduced to ~8 h). This orbit caused MESSENGER to make approximately vertical cuts through the magnetotail plasma sheet several times a day during certain seasons. It is within ~25 of these plasma sheet crossings that the process was tested and developed. These crossings are located in the near-Mercury tail, close to midnight in the tail plasma sheet. Orbits were carefully selected to ensure that the detections were related to flux ropes and not to other processes that occur closer to the magnetopause.

The magnetometer data were used in the aberrated Mercury-Solar-Magnetospheric (henceforth MSM) coordinate system. In this Cartesian system the $z$ axis ($\hat{Z}_{MSM}$) is aligned with the dipole axis pointing north, the $x$ direction ($\hat{X}_{MSM}$) traces the Mercury-Sun direction, and the $y$ axis ($\hat{Y}_{MSM}$) completes the right-handed set.

At Mercury the dipole and rotational axes are approximately aligned; however, the magnetic equatorial plane (described by $\hat{X}_{MSM}$ and $\hat{Y}_{MSM}$) is offset north from the planet's geometrical center by ~0.2 $R_M$ [*Anderson et al.*, 2011]. The magnetic field data were corrected for solar wind aberration (aberrated coordinates are indicated with "′" notation). This was accomplished using the local orbital velocity of Mercury and assuming a solar wind velocity of 425 km $s^{-1}$.

### 2.2. Magnetotail Flux Rope Signatures

Previous studies have found that flux ropes largely lie in the $\hat{X}$-$\hat{Y}$ plane [*Slavin et al.*, 2003a], generally with their axis in the $\pm\hat{Y}$ direction, traveling in the $\pm\hat{X}$ direction (planetward or tailward) due to the prevailing tail configuration [*DiBraccio et al.*, 2015]. If a flux rope were to pass directly over the spacecraft with this approximate orientation and velocity, then a magnetometer would observe: a bipolar variation in $B_Z$, a local maximum in $B_Y$ (corresponding to the strong core field along the axis), and a peak in the total field magnitude ($|B|$).

If the spacecraft passes directly through the center of a flux rope, then the deflection in $B_Z^{MSM}$ will be symmetrical and bipolar. However, if the spacecraft's passage through the flux rope is offset then the signature will be asymmetric and potentially unipolar. This is especially the case if only one "hemisphere" of the structure is encountered (i.e., the planetward or tailward side). We direct the reader to diagrams in *Borg et al.* [2012] and *DiBraccio et al.* [2015] showing the effect that trajectory can have on the magnetic signature of a plasmoid. The relative trajectories displayed are caused by a combination of the motion of the spacecraft and the current sheet. Differentiating between trajectories with large impact parameters and the traveling compression regions that surround the plasmoids as they interact with the lobes [*Slavin et al.*, 1993] will be accomplished using comparison to a model.

### 2.3. Force-Free Model

The force-free model represents a relatively stable configuration where no pressure gradients are assumed to be present ($\nabla P = 0$). In this model the magnetic pressure ($^{B^2}/_{2\mu_0}$) from the strong axial field is balanced by the magnetic tension force ($^{B^2}/_{2\mu_0 R_c}$), where $\mu_0$ is the magnetic permeability of free space and $R_c$ is the radius of curvature of the helical field. This corresponds to the lowest-energy state of helical magnetic fields and is therefore perhaps the end point of the evolution of the flux rope morphology [*Priest*, 1990]. Under these conditions, *Lepping et al.* [1990] showed that using the *Lundquist* [1950] solutions, the field inside the flux rope can be written in cylindrical coordinates as

$$B_{axial} = B_0 J_0(\alpha r') \tag{1}$$

$$B_{azimuthal} = B_0 H J_1(\alpha r') \tag{2}$$

$$B_r = 0 \tag{3}$$

where $B_0$ is the peak axial field strength, $J_0(\alpha r')$ and $J_1(\alpha r')$ are the zeroth- and first-order Bessel functions, and $H$ is the helicity or handedness of the flux rope ($H = \pm 1$). The Bessel functions depend on the radial distance from the axis of the flux rope ($r'$) and $\alpha$. With $\alpha$ set to 2.4048 [*Burlaga*, 1988], and setting the impact parameter: $r' = r/R_0$ (with $R_0$ being the radius of the flux rope) the model represents a flux rope with a completely axial field at the center ($B_{azimuthal}(r = 0) = 0$) and an entirely azimuthal field at the edge (($B_{axial}(r = R_0) = 0$)). This formulation represents a cylindrically symmetric, linear (constant $\alpha$) force-free flux rope. The model has been successfully applied to interplanetary magnetic clouds [*Lepping et al.*, 1990], FTEs at the magnetopause of Earth [*Eastwood et al.*, 2012a], Saturn [*Jasinski et al.*, 2016], and Mercury [*Imber et al.*, 2014] as well as flux ropes in the magnetotails of Earth [*Lepping et al.*, 1995, 1996; *Slavin et al.*, 2003a, 2003b], Mars [*Eastwood et al.*, 2012b], and Mercury [*DiBraccio et al.*, 2015].

The assumption that the flux rope is linearly (constant $\alpha$) force free and cylindrically symmetric will limit the number of flux ropes that are identified by the technique. As mentioned above, the model is likely to better represent well developed flux ropes. Flux ropes encountered soon after their formation are unlikely to have evolved to the stable equilibrium described by the model. Implications of this assumption are discussed in section 5.1.

## 3. Method

The technique, described below, uses three steps to locate quasi force-free flux ropes within spacecraft magnetometer data. The combination of all three ensures fully automated, rigorous, and repeatable flux rope detections.

### 3.1. Baseline Crossing and Peak Detection

The aim of the first step in the technique is to find significant deflections in the $B_Z$ component of the field concurrent with peaks in the $B_Y$, or $|B|$ components of the field. This field signature is discussed in section 2.2 as being the expected result of an equatorial magnetotail flux rope traveling sunward (or tailward) directly over the spacecraft.

This step is similar to the method developed by *Smith et al.* [2016] and is illustrated in Figure 1. Once identified, candidates will be further analyzed and ultimately accepted or rejected based on the results of the subsequent steps. The algorithm first takes a running average of the $B_Z$ component of the field within a 1 min sliding window. The window size was selected specifically for the Mercury data as it was found to trace the "long" term changes in the field but ignore sharp changes in the field (e.g., flux rope signatures). The running average forms a new baseline through which any deflections of the field must pass. Every instance where $B_Z$ passes through this baseline, henceforth referred to as a crossing, is recorded for further analysis.

To investigate whether the deflection of the field is significant, the method then searches for local maxima and minima of $B_Z$. Defining the event using the local north-south maxima of the field attempts to find the duration that would be chosen by eye, following the work of *Slavin et al.* [1993], and more recently *Jackman et al.* [2014], *Vogt et al.* [2014], *DiBraccio et al.* [2015], and *Smith et al.* [2016]. A period extending 1.25 s either side of the crossing (vertical grey bars in Figure 1) is examined to find these local extrema. This time window was chosen in order to preferentially select the fluctuations interpreted as flux ropes; *DiBraccio et al.* [2015] reported an average duration of 0.74 s.

If the deflection is southward, i.e., the value of $B_Z$ decreases, then all peaks in the field (where the field is larger than at adjacent points) up to 1.25 s before the crossing are selected as potential starts. On the other side, after the crossing, all local minima of the field (where the field is smaller or more negative than at adjacent points) up to 1.25 s after the crossing are selected as potential ends.

All possible combinations of potential starts and ends are then examined, with the aim of selecting the duration representing the largest and smoothest fluctuation. First-order polynomials are interpolated between the various pairs. The interpolations are then compared with the data using the coefficient of determination, given by

$$r^2 = 1 - \frac{\sum_0^N \left(B_Z^t - f_t\right)^2}{\sum_0^N \left(B_Z^t - \bar{B_Z}\right)^2} \tag{4}$$

The start and end pair is located at $t = 0$ and $t = N$, respectively. $B_Z^t$ is the value of $B_Z$ at the point $t$, $\bar{B_Z}$ is the average of $B_Z$ over all points included. Finally, $f_t$ is the value of the interpolation at time $t$. If all the data points lie precisely on the polynomial, this would yield an $r^2$ value of 1. The grey, red, and green lines on Figure 1 show the possible interpolations for the example event.

If the value of $r^2$ is less than 0.9 (e.g., as for the grey lines in Figure 1), and therefore the polynomial represents a poor fit to the data, then the start/end pair is discarded. The magnitude of the deflection, given by

$$\Delta B_Z = B_Z^0 - B_Z^N \tag{5}$$

is then evaluated for all pairs for which $0.9 \leq r^2 \leq 1$ (the green and red lines on Figure 1) using equation (5) ($B_Z^0$ and $B_Z^N$ being the value of the $B_Z$ component of the field at the start and end, respectively). The start/end pair with the largest absolute value of $\Delta B_Z$ is then selected, defining the event duration, shown by the green line in Figure 1. The method defines the limits of the event, shown by the vertical green bars in Figure 1. In this case the limits well match those that may have been selected by eye.

The magnitude of the deflection ($|\Delta B_Z|$) is then compared to the standard deviation of the field ($\sigma_{B_Z}$), requiring that

$$\frac{|\Delta B_Z|}{\sigma_{B_Z}} \geq 1 \tag{6}$$

where $\sigma_{B_Z}$ is calculated for the same 1 min sliding window as the average of $B_Z$. If equation (6) is satisfied, then the deflection is preliminarily accepted. This threshold is relatively low; however, the aim of this step is to find all possible deflections, so they may be evaluated by the following methods.

The event duration identified is then inspected for local peaks in $B_Y$, or $|B|$ using wavelet analysis. Figure 1 demonstrates this step. The green vertical bars indicate event duration as selected by the previous step.

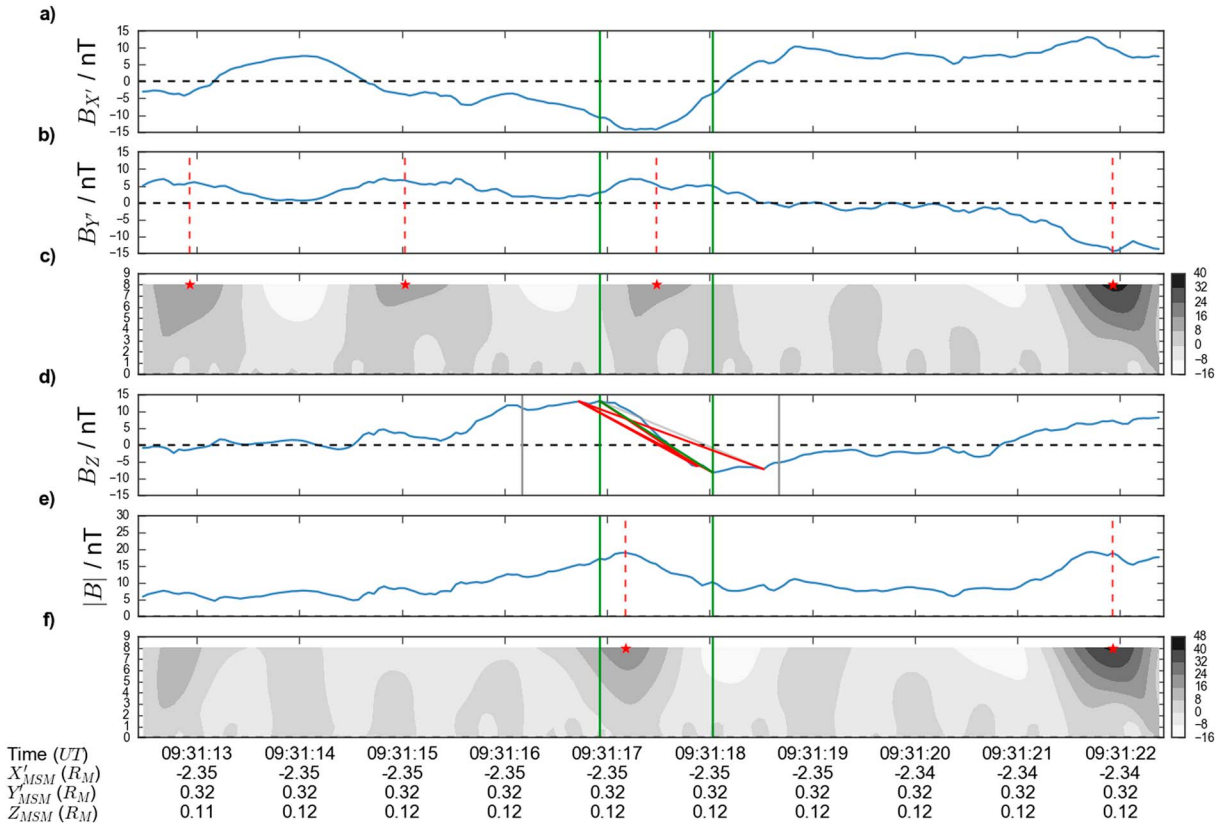


**Figure 1.** An example flux rope detection. (a, b, d, and e) The magnetic field in aberrated MSM coordinates. The grey vertical bars on Figure 1d indicate the maximum length of the event (±1.25 s). The faint grey lines show the first-order polynomials interpolated between the potential start/stop pairings that have a value of $r^2 < 0.9$. The red lines indicate those interpolated lines with an $r^2 \geq 0.9$ (calculated from equation (4)). The green line shows the final interpolated line selected; with an $r^2 \geq 0.9$ and the largest value of $\Delta B_Z$ (from equation (5)). The green vertical lines indicate the corresponding selected start and end to the deflection, respectively. (c and f) The Continuous Wavelet Transform (CWT) of $|B_{Y'}|$ and $|B|$, respectively (with the Ricker wavelet). The color bar indicates the value of the CWT coefficient, while the vertical axis shows the wavelet scale factor. The red stars indicate the locations of the significant peaks in the CWT. The red dashed lines then show the locations of the peaks in the panel of the relevant magnetic field component.

Figures 1c and 1f show the results of the Continuous Wavelet Transform (CWT) when applied to $|B_{Y'}|$ and $|B|$ (approximately Figures 1b and 1e), respectively, using the Ricker (or Mexican Hat/Marr) wavelet [*Daubechies*, 1992]. The Ricker wavelet is the normalized second derivative of a Gaussian function, importantly featuring a central peak. The CWT and Ricker wavelet combination are commonly used in various fields for pattern matching and peak detection [e.g., *Carmona et al.*, 1998; *Du et al.*, 2006]. Figures 1c and 1f display time on the horizontal axis and wavelet scale on the vertical axis. The colors indicate the value of the CWT coefficient: strongly positive where the wavelet (with a given scale) matches well with a peak in the data. Local peaks in the CWT coefficient are selected, and those greater than an empirical threshold (designed to preferentially select peaks with a small scale factor), are indicated with red stars. The red dashed lines then indicate the positions of these peaks in the panel of the corresponding component of the field.

If significant peaks are identified in either $B_{Y'}$ or $|B|$ (Figures 1b or 1e) within the duration indicated by the green bars then the deflection is accepted. Figure 1 shows an event for which peaks have been identified in both panels. However, only one peak is required as they can be missed by the CWT technique.

This combination of techniques recreates the by-eye selection criteria used by several previous studies [e.g., *Slavin et al.*, 2003a; *DiBraccio et al.*, 2015].

It is possible that the combination of $B_Z$ deflection and peak in $B_{Y'}$ or $|B|$ could be caused by other magnetic structures within the magnetotail. To remove such signatures, criteria are then placed on the results of both minimum variance analysis (MVA) and comparison to a model (sections 3.2 and 3.3).

### 3.2. Minimum Variance Analysis

The second stage of the process involves Minimum Variance Analysis (MVA); rotating the magnetic field data into a local coordinate system to further check for flux rope-like characteristics. If the magnetic signature is caused by a close encounter with a force-free flux rope, then it may be expected that the new coordinate system is distinct and that a clear rotation of the field is apparent (as will be discussed below) [*Slavin et al.*, 1989; *Briggs et al.*, 2011; *DiBraccio et al.*, 2015].

MVA was first developed to find the normal to magnetic discontinuities (e.g., current layers) from magnetometer data [*Sonnerup and Cahill*, 1967]. However, the technique has also been used to determine the orientation and structure of flux ropes (if the spacecraft passes sufficiently close to the axis and the flux rope satisfies the force-free approximation) [e.g., *Sibeck et al.*, 1984; *Elphic et al.*, 1986; *Slavin et al.*, 1989; *Moldwin and Hughes*, 1991; *Xiao et al.*, 2004].

MVA outputs three eigenvectors, representing the minimum, intermediate, and maximum variation directions ($\mathbf{e_1}$, $\mathbf{e_2}$, and $\mathbf{e_3}$ respectively), and three corresponding eigenvalues ($\lambda_1$, $\lambda_2$, and $\lambda_3$). The three eigenvalues are often quoted in two ratios: the maximum to intermediate ($\lambda_3/\lambda_2$) and the intermediate to minimum ($\lambda_2/\lambda_1$). The relative size of the eigenvalues describes how well the new coordinate system is defined (low ratios suggest the axes are more degenerate [*Khrabrov and Sonnerup*, 1998; *Sonnerup and Scheible*, 1998]), so we require for event acceptance that both of the ratios are greater than five. *Briggs et al.* [2011], at Mars, placed a limit on $\lambda_2/\lambda_1$ of 8, while *DiBraccio et al.* [2015] placed no limits on either ratio and found $\lambda_3/\lambda_2$ as low as 3, and $\lambda_2/\lambda_1$ always less than 12. *DiBraccio et al.* [2015] found that placing thresholds did not change their results and so chose to keep the larger sample for statistical reasons. For this study a threshold is used to help exclude poor quality events (as no manual preselection is performed). Requiring both ratios to be greater than 5 means all three eigenvectors are distinct. No criterion is placed upon the direction of the eigenvectors.

Additionally, the start and end times are varied (from those identified in section 3.1) by ±10% of the duration. MVA is performed on all the possible combinations of starts and ends this allows. The amount by which the maximum eigenvalue ratio changes is then calculated by the following:

$$\max\left(\lambda_3/\lambda_2\right)/\operatorname{mean}\left(\lambda_3/\lambda_2\right) \leq 1.75 \tag{7}$$

If the magnetic structure is well defined, and analysis stable, then the eigenvalue ratio should not change by a large amount, and equation (7) should be satisfied. The limit of 1.75 was determined empirically from running the analysis on the test current sheet crossings.

The pair for which the product of $\lambda_3/\lambda_2$ and $\lambda_2/\lambda_1$ is greatest is then selected, attempting to maximize both ratios (and thereby select the most distinct eigenvectors). Often, this is the same as the duration selected in the previous step of the pipeline, or differs by only one data point.

Finally, a clear rotation of the field in a hodogram of the intermediate and maximum field directions is expected when the spacecraft passes through a flux rope. To evaluate this property, an ellipse is fit using least squares minimization to the hodogram trace following the method of *Fitzgibbon et al.* [1999]. The quality of the fit to the data is evaluated using a modified $r^2$ (equation (8)):

$$r^2 = 1 - \frac{\sum_{i=0}^{N} a_i^2}{\sum_{i=0}^{N} c_i^2} \tag{8}$$

where the summations are over all data points ($i = 0$ to $N$), $a_i$ is the radial distance between the point $i$ and the ellipse (point $P$), and $c_i$ is the radial distance between the center and the point $P$ on the ellipse. If all points lie directly on the ellipse, then $r^2 = 1$. We require that the fit is of a good quality: i.e., $r^2 \geq 0.98$. The ellipse fitting technique requires at least four data points; this imposes a lower limit to the duration of flux rope that can be identified depending on the resolution of the data used. With the 20 Hz MESSENGER data, this is 0.2 s.

In addition, poor detections are characterized by highly eccentric ellipse fits; therefore, for acceptance, $e \leq 0.9$. The ellipse fitting technique is known to have a bias for producing ellipses with low eccentricities [*Fitzgibbon et al.*, 1999]; therefore, the fit should meet the criteria if possible.

Figure 2 shows the results of running MVA on the flux rope shown in Figure 1. The expected flux rope characteristics can be seen; little variation in $B1$ (the minimum variance direction), a peak (the core field) in $B2$, and an approximately bipolar signature in $B3$ (the maximum variance direction). If the spacecraft had passed

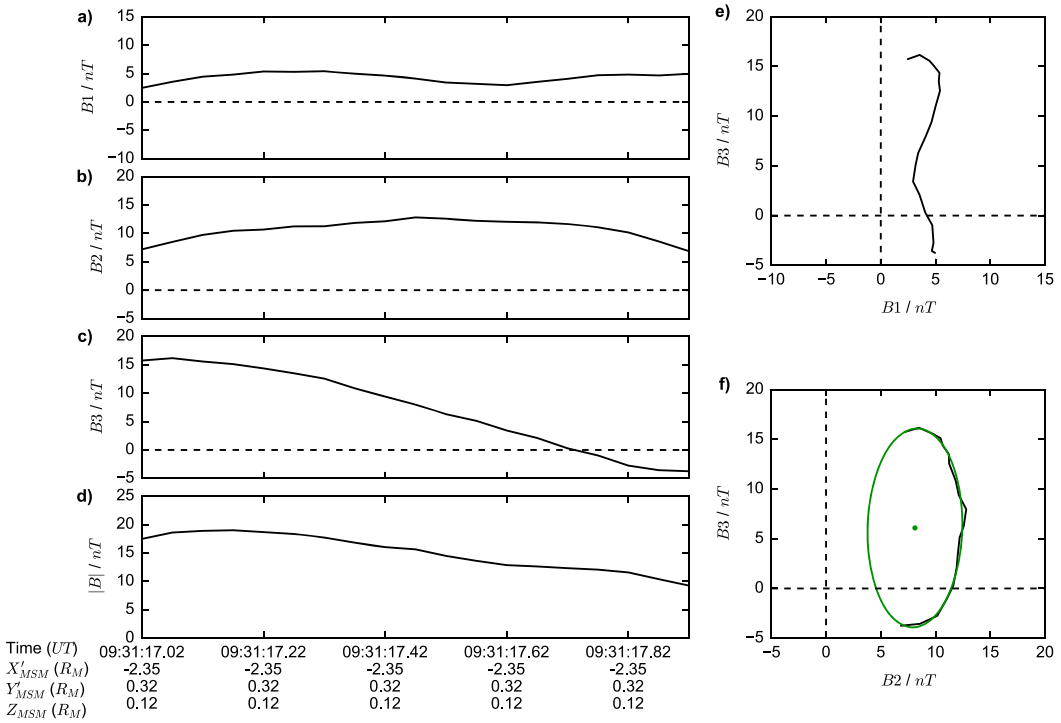


**Figure 2.** Results of the MVA analysis on the example flux rope shown in Figure 1. The magnetic field is shown in the MVA coordinate system, where B1, B2, and B3 are the field components in the minimum, intermediate, and maximum variance directions, respectively. Hodograms of the field are also shown. The hodogram displaying B2–B3 (Figure 2f) is overplotted with the result of the ellipse fitting in green (described in section 3.2); the green dot is the center of the fitted ellipse.

through the center of the flux rope, then $B1$ would be 0; $B1$ increases in magnitude as the impact parameter increases. The corresponding eigenvalue ratios are $\lambda_3/\lambda_2 = 13.68$ and $\lambda_2/\lambda_1 = 7.22$, with a calculated variation in the maximum to intermediate ratio of 1.383. These values demonstrate a well defined MVA coordinate system with distinct eigenvectors. The ellipse in the $B2-B3$ hodogram is a good fit ($r^2 = 0.996$) and is not highly eccentric ($e = 0.849$).

### 3.3. Force-Free Flux Rope Fitting

The third and final step of the pipeline attempts to fit the data to a model flux rope. Not only does this provide another set of criteria to exclude poor quality signatures but also allows an estimation of the core field and proximity of the spacecraft to the flux rope axis. The implications of the choice of model are discussed in section 5.1.

The aberrated magnetometer data, within the region identified in section 3.2, is rotated into MVA coordinates and normalized. From there it is transformed into flux rope axial and azimuthal coordinates. The intermediate variance direction is taken to correspond to the axial direction while the azimuthal direction is composed of a combination of the minimum and maximum variance directions. This implicitly assumes that the MVA technique has correctly located the axial direction. This is a good assumption at small impact parameters; however, it can be shown to become less valid as the impact parameter increases. Using the force-free model, an impact parameter of 0.5 $R_0$ results in an angular difference between the intermediate direction and axial direction of ~20° [*Xiao et al.*, 2004].

The modeled magnetic field of the flux rope, shown in equations (1) and (2), is normalized and computed for impact parameters between 0 and 0.95 (Impact Parameter = $r/R_0$). The results are then compared to the data using a modified $\chi^2$ ($\chi_1^2$), shown in equation (9), as in *DiBraccio et al.* [2015]:

$$\chi_1^2 = \frac{\sum \left( \left( B_{\text{Axial}}^{\text{Data}} - B_{\text{Axial}}^{\text{Model}} \right)^2 + \left( B_{\text{Azimuthal}}^{\text{Data}} - B_{\text{Azimuthal}}^{\text{Model}} \right)^2 \right)}{N} \tag{9}$$

where the sum is over all $N$ data points, $B^{\text{Data}}_{\text{Axial}}$ and $B^{\text{Data}}_{\text{Azimuthal}}$ are the normalized axial and azimuthal components of the field and $B^{\text{Model}}_{\text{Axial}}$ and $B^{\text{Model}}_{\text{Azimuthal}}$ are the normalized axial and azimuthal results of the model. The model is compared to the MVA duration defined in section 3.2; however, the fit is allowed to ignore up to the first and last 20% of the data points if this provides a better fit. This flexibility is somewhat analogous to *Slavin et al.* [2003a] allowing the time of closest approach to vary in their fitting. The impact parameter, and duration, with the smallest $\chi_1^2$ is then selected as the best fit. For the flux rope in Figures 1 and 2 the best fit $\chi_1^2$ (of 0.062) was obtained at an impact parameter of 0.33 $R_0$.

Once the best fit to the normalized data has been computed, the result is rotated back into MVA coordinates. Another measure of $\chi^2$ is then evaluated comparing the three-dimensional fit with the data; $\chi_2^2$ is shown in equation (10) (similar to that used by *Lepping et al.* [1990]):

$$\chi_2^2 = \frac{\sum \left( (B_1^{\text{Data}} - B_1^{\text{Model}})^2 + (B_2^{\text{Data}} - B_2^{\text{Model}})^2 + (B_3^{\text{Data}} - B_3^{\text{Model}})^2 \right)}{3N - n} \tag{10}$$

where the sum is over all $N$ data points; the differences between all three normalized minimum variance components of the field (as defined in section 3.2) and the model results are calculated and squared. The factor of $n$ here represents the number of free parameters in the fit (taken to be four). For the example flux rope (in Figures (1) and (2)) the value of $\chi_2^2$ calculated was 0.048. The peak axial field calculated by the model is then scaled to equal the peak axial field found in the MVA analysis to provide an estimate of $B_0$: the core field strength. With the scaling completed, the result can be rotated back into MSM coordinates.

With the data compared to the model results we place requirements both on the quality of the fit ($\chi^2$) and the best fit impact parameter (IP). If the IP is larger than 0.5 $R_0$ then the MVA technique should be less able to distinguish the axial orientation, and so the events are rejected. In addition, we require that either $\chi_1^2$ or $\chi_2^2$ is less than 0.15 (so the flux rope can be well modeled as linearly force free). Normally, the two values of $\chi^2$ are approximately the same.

## 4. Application

To test the efficacy of the method, it has been applied to the same data set as that previously investigated by *DiBraccio et al.* [2015]. During 30 MESSENGER magnetotail current sheet encounters, between 2011 and 2013, *DiBraccio et al.* [2015] identified a total of 49 flux ropes. The three-step process independently reidentifies eight of these. Nineteen of the flux ropes identified by *DiBraccio et al.* [2015] do not possess greater than 1$\sigma$ deflections of the field in the $B_Z$ component and so are not located by the first step (though they do exhibit significant peaks in $B_Y$ and $|B|$). The remaining flux ropes that are not selected by the method are split evenly between those that did not meet the required MVA criteria and those that did not fit the force-free model to the required accuracy (or did but for impact parameters $\geq 0.5\,R_0$).

Figure 3 shows the result of the application of the method to two example passages of MESSENGER through the Hermean cross-tail current sheet on 23 and 24 November 2011. The magnetic field is provided in aberrated MSM coordinates. The flux ropes identified by this method are shaded green. Those identified by *DiBraccio et al.* [2015] and missed by our method are highlighted in red. Figure 3 (top), showing data from 23 November 2011, was recorded during a period of high-solar wind dynamic pressure (due to the impact of a coronal mass ejection) [*Slavin et al.*, 2014]. This caused compression of the dayside magnetopause and very high rates of reconnection on the dayside. Correspondingly, a high rate of flux rope formation and ejection is observed. One flux rope identified by *DiBraccio et al.* [2015] is not recovered around 09 : 25 : 40 due to a large variation in the MVA eigenvalues observed (violating the criterion in equation (7)). In Figure 3 (bottom) a flux rope identified by *DiBraccio et al.* [2015] is not selected due to a large best fit impact parameter ($\geq 0.5\,R_0$).

To further validate the technique, it was applied to data from Earth's magnetotail: from the Cluster [*Escoubet et al.*, 1997; *Balogh et al.*, 2001; *Laakso et al.*, 2010] and Geotail [*Mukai et al.*, 1994] missions. The method was tested to check if it could recover events from the figures of previous studies. Adapting it for the different timescales, the method identifies both flux ropes shown by *Slavin et al.* [2003a]. Three out of four flux ropes shown by *Borg et al.* [2012] are initially located, though two of these are then discarded as they do not fit the model satisfactorily at the required impact parameters. Both flux ropes shown by *Zhao et al.* [2016] are located; however, one is later discarded as it does not sufficiently fit the model.

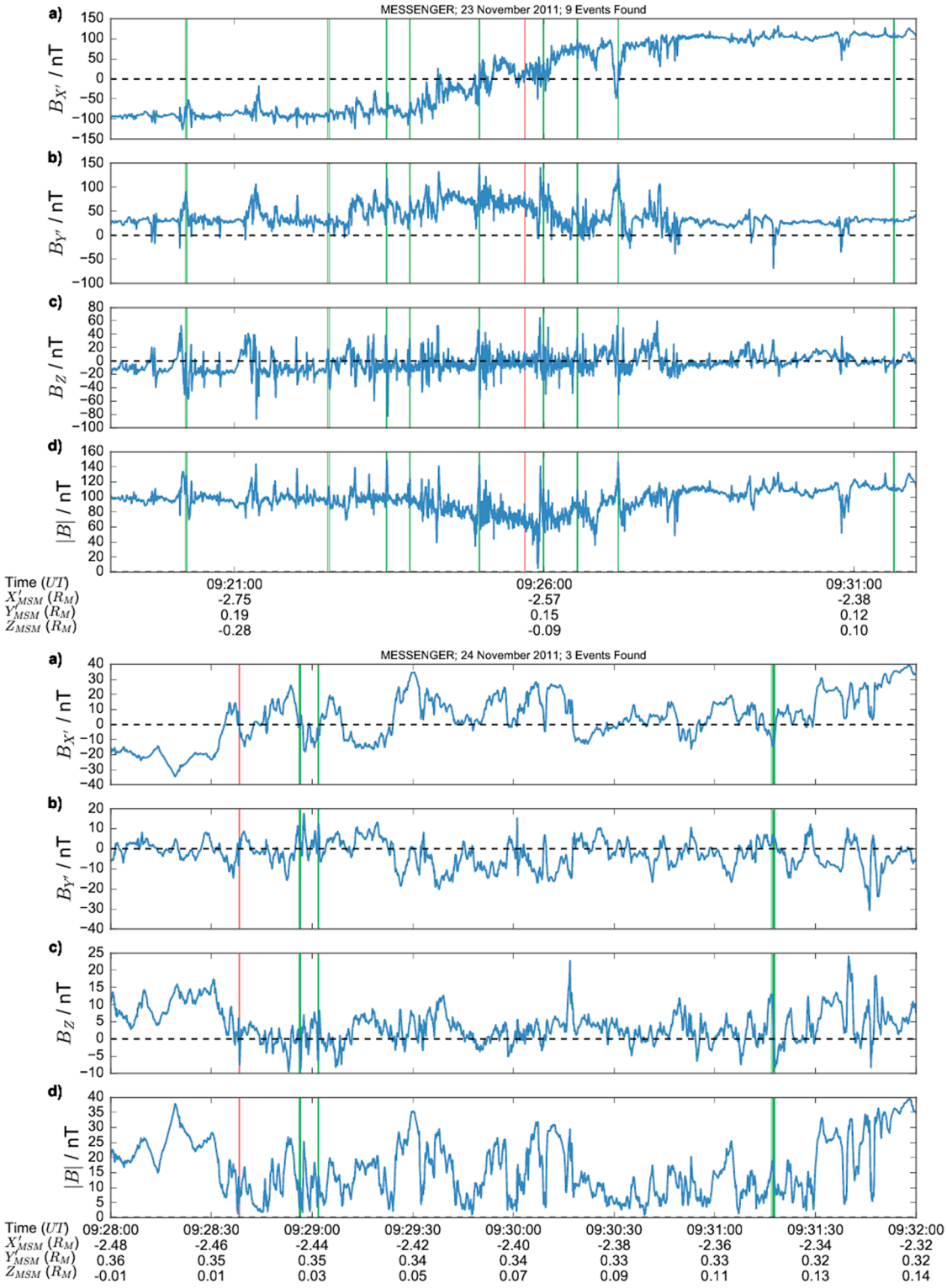


**Figure 3.** Two example MESSENGER passages through the Hermean magnetotail current sheet. Magnetic field is provided in aberrated MSM coordinates. Positive force-free flux rope detections by the method are indicated with green shading. Flux ropes identified by *DiBraccio et al.* [2015] but missed by this technique are highlighted in red.

## 5. Discussion

The method described above represents an automated, consistent method of identifying in situ encounters with cylindrically symmetric, linear (constant $\alpha$) flux ropes within spacecraft magnetometer data. In the section below several key assumptions that the process makes are outlined and potential future adaptations are discussed.

### 5.1. Assumptions

The first major assumption made by the process is that the MVA process has correctly determined the orientation of the flux rope. This has been shown in the past to be true in some situations, and to be a better approximation when the spacecraft passes close to the axis [*Xiao et al.*, 2004]. If MVA fails to correctly locate the axial direction, then the event will appear to be a poor fit to the model and the flux rope will probably not be identified.

Second, the force-free model applied assumes that the flux rope is cylindrically symmetrical. It is probable that most flux ropes are in some way distorted through interactions with the surrounding field and plasma. There are alternative models that allow for some deformation, for example, those that allow an elliptical or oblate flux rope [e.g., *Hidalgo et al.*, 2002 and *Vandas and Romashets*, 2003]. While these models allow more accurate fits of distorted flux ropes, they also introduce more free parameters. The purpose of the fit is to provide additional criteria to rule out poor flux rope candidates and allow the estimation of some key parameters. More complex models could be subsequently fit to the successful candidate flux ropes to discern more information about their structure.

Finally, the chosen model assumes that the flux rope is (constant $\alpha$) force free; this will result in the exclusion of some flux ropes from the analysis. In fact, as mentioned in section 2.3, the model is likely to be a poor fit to flux ropes that are encountered soon after their formation. This will almost certainly introduce a selection effect. However, without access to high-resolution plasma data any model that includes the internal plasma pressure within a flux rope would be poorly constrained. This could result in the inclusion of poor quality events if the plasma parameters that are assumed are not representative of the true environment.

### 5.2. Adaptation

The analysis outlined above could be applied to other large data sets and used to create a self-consistent catalog of quasi force-free flux ropes. If used at other planets, the times scales used would require adjustment; i.e., the maximum length of event and duration over which the averages are calculated. Additionally, if simultaneous high-resolution plasma data are available, then this could be used to create additional criteria (or modify existing ones). Furthermore, such plasma data would also allow more complex analysis techniques to be employed (e.g., the method of *Rong et al.* [2013] for determining axis orientation). Finally, the method could be applied to virtual spacecraft simulation results, which can shed light on the limitations of in situ spacecraft detections.

## 6. Conclusion

We have presented a completely automated method of locating cylindrically symmetric, linear (constant $\alpha$) flux ropes from spacecraft magnetometer data. The analysis initially identifies significant ($\Delta B_Z \geq 1\sigma$) deflections in the north-south component of the magnetic field concurrent with peaks in the dawn-dusk component or total field. These candidates are then inspected using MVA to select those for which it is able to determine a well defined coordinate system with a clear rotation of the field. Those identified are then compared to a force-free model and the quality of the fit evaluated. The fitting of a model to the magnetic signature allows both the rejection of poor quality events (those likely due to other processes) and the determination of some of the physical parameters of the flux rope (i.e., the radius of the flux rope and core field strength). The pipeline has been tested on data from the MESSENGER mission and successfully relocates several previously studied flux ropes from *DiBraccio et al.* [2015]. It has also been applied to Earth data from Geotail and Cluster and recovers some prominent examples from the literature [*Slavin et al.*, 2003a; *Borg et al.*, 2012; *Zhao et al.*, 2016]. The method is ideal for application to large data sets whose manual inspection would be time consuming and include unknown biases.

**Acknowledgments**
The data used in this study were available from the Planetary Data System (PDS): http://pds.jpl.nasa.gov. A.W.S. is funded by a SEPnet PhD studentship. C.M.J. is supported by STFC Ernest Rutherford Fellowship ST/L004399/1. R.C.F. is supported by STFC Ernest Rutherford Fellowship ST/K004298/2. G.A.D. is supported by a NASA Postdoctoral Program appointment at the NASA Goddard Space Flight Center, administered by Universities Space Research Association through a contract with NASA. L.T. is supported by STFC Ernest Rutherford grant ST/L002809/1. Cluster data used in this paper were downloaded from the European Space Agency's Cluster and Double Star Science Archive (http://www.cosmos.esa.int/web/csa/access). Geotail magnetic field (electric field and/or plasma) data were provided by T. Nagai (H. Hayakawa and/or Y. Saito) through DARTS at Institute of Space and Astronautical Science, JAXA in Japan.

## References

Akasofu, S.-I. (1964), The development of the auroral substorm, *Planet. Space Sci.*, *12*(4), 273–282, doi:10.1016/0032-0633(64)90151-5.
Anderson, B., M. Acuña, D. Lohr, J. Scheifele, A. Raval, H. Korth, and J. Slavin (2007), The magnetometer instrument on MESSENGER, *Space Sci. Rev.*, *131*(1–4), 417–450, doi:10.1007/s11214-007-9246-7.
Anderson, B. J., C. L. Johnson, H. Korth, M. E. Purucker, R. M. Winslow, J. A. Slavin, S. C. Solomon, R. L. McNutt, J. M. Raines, and T. H. Zurbuchen (2011), The global magnetic field of Mercury from MESSENGER orbital observations, *Science*, *333*(6051), 1859–1862, doi:10.1126/science.1211001.
Baker, D. N., T. I. Pulkkinen, V. Angelopoulos, W. Baumjohann, and R. L. McPherron (1996), Neutral line model of substorms: Past results and present view, *J. Geophys. Res.*, *101*(A6), 12,975–13,010, doi:10.1029/95JA03753.
Balogh, A., et al. (2001), The Cluster magnetic field investigation: Overview of in-flight performance and initial results, *Ann. Geophys.*, *19*(10–12), 1207–1217, doi:10.5194/angeo-19-1207-2001.
Borg, A. L., M. Taylor, and J. P. Eastwood (2012), Observations of magnetic flux ropes during magnetic reconnection in the Earth's magnetotail, *Ann. Geophys.*, *30*(5), 761–773.
Briggs, J. A., D. A. Brain, M. L. Cartwright, J. P. Eastwood, and J. S. Halekas (2011), A statistical study of flux ropes in the Martian magnetosphere, *Planet. Space Sci.*, *59*(13), 1498–1505, doi:10.1016/j.pss.2011.06.010.
Burlaga, L. F. (1988), Magnetic clouds and force-free fields with constant alpha, *J. Geophys. Res.*, *93*(A7), 7217–7224, doi:10.1029/JA093iA07p07217.
Carmona, R., W. L. Hwang, and B. Torresani (1998), *Practical Time-Frequency Analysis: Gabor and Wavelet Transforms, with an Implementation in S, Wavelet Anal. and Its Appl.*, Elsevier Sci., San Diego, Calif.
Cowley, S. W. H. (1981), Magnetospheric asymmetries associated with the y-component of the IMF, *Space Sci. Rev.*, *29*, 79–96.
Daubechies, I. (1992), *Ten Lectures on Wavelets*, vol. 61, SIAM, Philadelphia, Pa.
DiBraccio, G. A., et al. (2015), MESSENGER observations of flux ropes in Mercury's magnetotail, *Planet. Space Sci.*, *115*, 77–89, doi:10.1016/j.pss.2014.12.016.
Du, P., W. A. Kibbe, and S. M. Lin (2006), Improved peak detection in mass spectrum by incorporating continuous wavelet transform-based pattern matching, *Bioinformatics*, *22*(17), 2059–2065, doi:10.1093/bioinformatics/btl355.
Dungey, J. W. (1961), Interplanetary magnetic field and the auroral zones, *Phys. Rev. Lett.*, *6*, 47–48.
Eastwood, J. P., T. D. Phan, R. C. Fear, D. G. Sibeck, V. Angelopoulos, M. Øieroset, and M. A. Shay (2012a), Survival of flux transfer event (FTE) flux ropes far along the tail magnetopause, *J. Geophys. Res.*, *117*, A08222, doi:10.1029/2012JA017722.
Eastwood, J. P., J. J. H. Videira, D. A. Brain, and J. S. Halekas (2012b), A chain of magnetic flux ropes in the magnetotail of Mars, *Geophys. Res. Lett.*, *39*, L03104, doi:10.1029/2011GL050444.
Elphic, R. C., C. A. Cattell, K. Takahashi, S. J. Bame, and C. T. Russell (1986), ISEE-1 and 2 observations of magnetic flux ropes in the magnetotail: FTE's in the plasma sheet?, *Geophys. Res. Lett.*, *13*(7), 648–651, doi:10.1029/GL013i007p00648.
Escoubet, C. P., R. Schmidt, and M. L. Goldstein (1997), Cluster—Science and mission overview, in *Space Science Reviews*, vol. 79, 1st ed., edited by C. P. Escoubet, R. Schmidt, and C. T. Russell, pp. 11–32, Springer, Netherlands, doi:10.1023/A:1004923124586.
Fitzgibbon, A., M. Pilu, and R. B. Fisher (1999), Direct least squares fitting of ellipses, *IEEE Trans. Pattern Anal. Mach. Intell.*, *21*(5), 476–480.
Hidalgo, M. A., T. Nieves-Chinchilla, and C. Cid (2002), Elliptical cross-section model for the magnetic topology of magnetic clouds, *Geophys. Res. Lett.*, *29*(13), 14–15, doi:10.1029/2001GL013875.
Huang, C.-S. (2002), Evidence of periodic (2–3 hour) near-tail magnetic reconnection and plasmoid formation: Geotail observations, *Geophys. Res. Lett.*, *29*(24), 42–44, doi:10.1029/2002GL016162.
Hughes, W. J., and D. G. Sibeck (1987), On the 3-dimensional structure of plasmoids, *Geophys. Res. Lett.*, *14*(6), 636–639, doi:10.1029/GL014i006p00636.
Ieda, A., S. Machida, T. Mukai, Y. Saito, T. Yamamoto, A. Nishida, T. Terasawa, and S. Kokubun (1998), Statistical analysis of the plasmoid evolution with Geotail observations, *J. Geophys. Res.*, *103*(A3), 4453–4465, doi:10.1029/97JA03240.
Imber, S. M., J. A. Slavin, S. A. Boardsen, B. J. Anderson, H. Korth, R. L. McNutt, and S. C. Solomon (2014), MESSENGER observations of large dayside flux transfer events: Do they drive Mercury's substorm cycle?, *J. Geophys. Res. Space Physics*, *119*, 5613–5623, doi:10.1002/2014JA019884.
Jackman, C. M., et al. (2014), Saturn's dynamic magnetotail: A comprehensive magnetic field and plasma survey of plasmoids and traveling compression regions and their role in global magnetospheric dynamics, *J. Geophys. Res. Space Physics*, *119*, 5465–5494, doi:10.1002/2013JA019388.
Jasinski, J. M., J. A. Slavin, C. S. Arridge, G. Poh, X. Jia, N. Sergis, A. J. Coates, G. H. Jones, and J. Hunter Waite (2016), Flux transfer event observation at Saturn's dayside magnetopause by the Cassini spacecraft, *Geophys. Res. Lett.*, *43*, 6713–6723, doi:10.1002/2016GL069260.
Karimabadi, H., T. B. Sipes, Y. Wang, B. Lavraud, and A. Roberts (2009), A new multivariate time series data analysis technique: Automated detection of flux transfer events using Cluster data, *J. Geophys. Res.*, *114*, A06216, doi:10.1029/2009JA014202.
Karimabadi, H., T. B. Sipes, H. White, M. Marinucci, A. Dmitriev, J. K. Chao, J. Driscoll, and N. Balac (2007), Data mining in space physics: MineTool algorithm, *J. Geophys. Res.*, *112*, A11215, doi:10.1029/2006JA012136.
Kawano, H., and C. T. Russell (1996), Survey of flux transfer events observed with the ISEE 1 spacecraft: Rotational polarity and the source region, *J. Geophys. Res.*, *101*(A12), 27,299–27,308, doi:10.1029/96JA02703.
Khrabrov, A. V., and B. U. Ö. Sonnerup (1998), Error estimates for minimum variance analysis, *J. Geophys. Res.*, *103*(A4), 6641–6651, doi:10.1029/97JA03731.
Laakso, H., C. Perry, S. McCaffrey, D. Herment, A. J. Allen, C. C. Harvey, C. P. Escoubet, C. Gruenberger, M. G. G. T. Taylor, and R. Turner (2010), The Cluster active archive: Overview, in *The Cluster Active Archive*, edited by H. Laakso, M. Taylor, and C. P. Escoubet, pp. 3–37, Springer, Netherlands, doi:10.1007/978-90-481-3499-1.
Lepping, R. P., J. A. Jones, and L. F. Burlaga (1990), Magnetic field structure of interplanetary magnetic clouds at 1 AU, *J. Geophys. Res.*, *95*(A8), 11,957–11,965.
Lepping, R. P., J. A. Slavin, M. Hesse, J. A. Jones, and A. Szabo (1996), Analysis of magnetotail flux ropes with strong core fields: ISEE 3 observations, *J. Geomagn. Geoelectr.*, *48*(5), 589–601.
Lepping, R. P., D. H. Fairfield, J. Jones, L. A. Frank, W. R. Paterson, S. Kokubun, and T. Yamamoto (1995), Cross-tail magnetic flux ropes as observed by the GEOTAIL spacecraft, *Geophys. Res. Lett.*, *22*(10), 1193–1196, doi:10.1029/94GL01114.
Lundquist, S. (1950), Magnetohydrostatic fields, *Ark. Fys*, *2*, 361–365.
Malaspina, D. M., and J. T. Gosling (2012), Two spacecraft observations of magnetic discontinuities in the solar wind with STEREO, *J. Geophys. Res.*, *117*, A04109, doi:10.1029/2011JA017375.
Moldwin, M. B., and W. J. Hughes (1991), Plasmoids as magnetic flux ropes, *J. Geophys. Res.*, *96*(A8), 14,051–14,064, doi:10.1029/91JA01167.

Moldwin, M. B., and W. J. Hughes (1992), On the formation and evolution of plasmoids: A survey of ISEE 3 Geotail data, *J. Geophys. Res.*, *97*(A12), 19,259–19,282, doi:10.1029/92ja01598.
Mukai, T., S. Machida, Y. Saito, M. Hirahara, T. Terasawa, N. Kaya, T. Obara, M. Ejiri, and A. Nishida (1994), The low energy particle (LEP) experiment onboard the GEOTAIL satellite, *J. Geomagn. Geoelectr.*, *46*(8), 669–692, doi:10.5636/jgg.46.669.
Priest, E. R. (1990), The equilibrium of magnetic flux ropes, in *Physics of Magnetic Flux Ropes, Geophys. Monogr. Ser.*, vol. 58, edited by C. T. Russell, E. R. Priest, and L. C. Lee, pp. 1–22, AGU, Washington, D. C.
Richardson, I. G., S. W. H. Cowley, E. W. Hones, and S. J. Bame (1987), Plasmoid-associated energetic ion bursts in the deep geomagnetic tail—Properties of plasmoids and the postplasmoid plasma sheet, *J. Geophys. Res.*, *92*(A9), 9997–10,013.
Rong, Z. J., W. X. Wan, C. Shen, T. L. Zhang, A. T. Y. Lui, Y. Wang, M. W. Dunlop, Y. C. Zhang, and Q. G. Zong (2013), Method for inferring the axis orientation of cylindrical magnetic flux rope based on single-point measurement, *J. Geophys. Res. Space Physics*, *118*, 271–283, doi:10.1029/2012JA018079.
Schindler, K. (1974), A theory of the substorm mechanism, *J. Geophys. Res.*, *79*(19), 2803–2810, doi:10.1029/JA079i019p02803.
Scholer, M., G. Gloeckler, D. Hovestadt, B. Klecker, and F. M. Ipavich (1984), Characteristics of plasmoidlike structures in the distant magnetotail, *J. Geophys. Res.*, *89*(A10), 8872–8876, doi:10.1029/JA089iA10p08872.
Sibeck, D. G., G. L. Siscoe, J. A. Slavin, E. J. Smith, S. J. Bame, and F. L. Scarf (1984), Magnetotail flux ropes, *Geophys. Res. Lett.*, *11*(10), 1090–1093, doi:10.1029/GL011i010p01090.
Siscoe, G. L., N. F. Ness, and C. M. Yeates (1975), Substorms on Mercury?, *J. Geophys. Res.*, *80*(31), 4359–4363, doi:10.1029/JA080i031p04359.
Slavin, J. A., et al. (1989), CDAW 8 observations of plasmoid signatures in the geomagnetic tail: An assessment, *J. Geophys. Res.*, *94*(A11), 15,153–15,175, doi:10.1029/JA094iA11p15153.
Slavin, J. A., M. F. Smith, E. L. Mazur, D. N. Baker, E. W. Hones, T. Iyemori, and E. W. Greenstadt (1993), ISEE 3 observations of traveling compression regions in the Earth's magnetotail, *J. Geophys. Res.*, *98*(A9), 15,425–15,446.
Slavin, J. A., R. P. Lepping, J. Gjerloev, D. H. Fairfield, M. Hesse, C. J. Owen, M. B. Moldwin, T. Nagai, A. Ieda, and T. Mukai (2003a), Geotail observations of magnetic flux ropes in the plasma sheet, *J. Geophys. Res.*, *108*(A1), 1015, doi:10.1029/2002JA009557.
Slavin, J. A., et al. (2003b), Cluster electric current density measurements within a magnetic flux rope in the plasma sheet, *Geophys. Res. Lett.*, *30*(7), 1362, doi:10.1029/2002GL016411.
Slavin, J. A., et al. (2009), MESSENGER observations of magnetic reconnection in Mercury's magnetosphere, *Science*, *324*(5927), 606–610.
Slavin, J. A., et al. (2010), MESSENGER observations of extreme loading and unloading of Mercury's magnetic tail, *Science*, *329*(5992), 665–668, doi:10.1126/science.1188067.
Slavin, J. A., et al. (2012), MESSENGER and Mariner 10 flyby observations of magnetotail structure and dynamics at Mercury, *J. Geophys. Res.*, *117*, A01215, doi:10.1029/2011JA016900.
Slavin, J. A., et al. (2014), MESSENGER observations of Mercury's dayside magnetosphere under extreme solar wind conditions, *J. Geophys. Res. Space Physics*, *119*, 8087–8116, doi:10.1002/2014JA020319.
Smith, A. W., C. M. Jackman, and M. F. Thomsen (2016), Magnetic reconnection in Saturn's magnetotail: A comprehensive magnetic field survey, *J. Geophys. Res. Space Physics*, *121*, 2984–3005, doi:10.1002/2015JA022005.
Solomon, S. C., R. L. McNutt Jr., R. E. Gold, and D. L. Domingue (2007), MESSENGER mission overview, *Space Sci. Rev.*, *131*(1–4), 3–39.
Sonnerup, B. U. Ö., and L. J. Cahill (1967), Magnetopause structure and attitude from Explorer 12 observations, *J. Geophys. Res.*, *72*(1), 171–183, doi:10.1029/JZ072i001p00171.
Sonnerup, B. U. Ö., and M. Scheible (1998), Minimum and maximum variance analysis, in *Analysis Methods for Multi-Spacecraft Data, ISSI Sci. Rep. SR-001*, edited by G. Paschmann and P. W. Daly, pp. 185–220, ESA Publications Division, Noordwijk, Netherlands.
Sun, W.-J., et al. (2015), MESSENGER observations of magnetospheric substorm activity in Mercury's near magnetotail, *Geophys. Res. Lett.*, *42*(10), 3692–3699, doi:10.1002/2015GL064052.
Vandas, M., and E. P. Romashets (2003), A force-free field with constant alpha in an oblate cylinder: A generalization of the Lundquist solution, *Astron. Astrophys.*, *398*(3), 801–807.
Vasquez, B. J., V. I. Abramenko, D. K. Haggerty, and C. W. Smith (2007), Numerous small magnetic field discontinuities of Bartels rotation 2286 and the potential role of Alfvénic turbulence, *J. Geophys. Res.*, *112*, A11102, doi:10.1029/2007JA012504.
Vogt, M. F., M. G. Kivelson, K. K. Khurana, S. P. Joy, and R. J. Walker (2010), Reconnection and flows in the Jovian magnetotail as inferred from magnetometer observations, *J. Geophys. Res.*, *115*, A06219, doi:10.1029/2009JA015098.
Vogt, M. F., C. M. Jackman, J. A. Slavin, E. J. Bunce, S. W. H. Cowley, M. G. Kivelson, and K. K. Khurana (2014), Structure and statistical properties of plasmoids in Jupiter's magnetotail, *J. Geophys. Res. Space Physics*, *119*, 821–843, doi:10.1002/2013JA019393.
Xiao, C. J., Z. Y. Pu, Z. W. Ma, S. Y. Fu, Z. Y. Huang, and Q. G. Zong (2004), Inferring of flux rope orientation with the minimum variance analysis technique, *J. Geophys. Res.*, *109*, A11218, doi:10.1029/2004JA010594.
Zhao, Y., R. Wang, and A. Du (2016), Characteristics of field-aligned currents associated with magnetic flux ropes in the magnetotail: A statistical study, *J. Geophys. Res. Space Physics*, *121*, 3264–3277, doi:10.1002/2015JA022144.